

Article

Volumic Eddy-Current Losses in Conductive Massive Parts with Experimental Validations

Antony Plait  and Frédéric Dubas * 

Département ENERGIE, FEMTO-ST, CNRS, University Bourgogne Franche-Comté, F90000 Belfort, France

* Correspondence: frederic.dubas@univ-fcomte.fr; Tel.: +33-38-458-3648

Abstract: In this paper, the analytical determination of volumic eddy-current losses in rectangular-shaped conductive massive parts is presented with experimental validations. Eddy currents, as well as the resulting volumic losses, are generated by a sinusoidal spatially uniform applied magnetic field. A U-shaped electromagnetic device with a flat mobile armature (or adjustable air gap) is used to measure the eddy-current losses. The experimental device, its instrumentation, and the conductive massive parts are presented in detail in the paper. Thereafter, the magnetic field distribution applied on the conductive massive parts, which is the mean input data for the eddy-current loss model, is studied. A two-dimensional (2D) numerical model, under the FEMM software, for the magnetic field calculation was also developed. A comparative analysis between the experimental measurements and the numerical results allowed the distribution of the applied magnetic field to be accurately validated. In the final phase, the objective was to estimate the volumic eddy-current losses in rectangular-shaped aluminium conductive massive parts generated by the variation of this applied magnetic field. An analytical model, based on the Maxwell–Fourier method, for the accurate prediction of eddy-current losses has also been developed. An electromagnet with and without the conductive massive parts is characterized in terms of power consumption. By using the power conservation method (i.e., Boucherot’s theorem), the eddy-current losses could be quantified experimentally. The influence of segmentation is also studied. The analytical results are compared to the experimental test results.



Citation: Plait, A.; Dubas, F. Volumic Eddy-Current Losses in Conductive Massive Parts with Experimental Validations. *Energies* **2022**, *15*, 9413. <https://doi.org/10.3390/en15249413>

Academic Editor: Andrea Mariscotti

Received: 15 October 2022
Accepted: 8 December 2022
Published: 12 December 2022

Publisher’s Note: MDPI stays neutral with regard to jurisdictional claims in published maps and institutional affiliations.



Copyright: © 2022 by the authors. Licensee MDPI, Basel, Switzerland. This article is an open access article distributed under the terms and conditions of the Creative Commons Attribution (CC BY) license (<https://creativecommons.org/licenses/by/4.0/>).

Keywords: analytical model; eddy-current losses; experimental validation; instrumentation; magnetic field distribution; numerical analysis; segmentation effect

1. Introduction

1.1. Preamble

Over the past few decades, eddy-current losses have attracted a lot of interest in the scientific community [1–3]. The magnetic field is one of the most important quantities that influence the distribution of volumic eddy-current losses. Eddy currents, as well as resulting volumic losses, are generated in any conductive material located in a spatio-temporal varying magnetic field. The magnetic field variation is due to either its alternating nature or the relative movement of the material with respect to the source of the magnetic field, or both. Eddy currents involve volumic losses and consequently thermal heating in conductive massive parts [4], which could deteriorate system efficiency and performance. For example, magnets used in electrical machines, especially rare-earth magnets, having a high electrical conductivity (such as NdFeB or SmCo), are sensitive to temperature, which may cause their partial or irreversible demagnetization [5]. The skin depth δ of the material (characterized by the excitation frequency f , the electrical conductivity σ , and the absolute magnetic permeability of the material μ), which is defined by

$$\delta = \sqrt{\frac{2}{\mu \cdot \sigma \cdot \omega}} \text{ with } \omega = 2\pi \cdot f, \quad (1)$$

where ω is the electrical angular frequency, also influences the generated eddy-current losses. This will be detailed in this article.

Detailed states-of-the-art of the eddy-current loss models were realized in the studies reported in [6–10]. The mathematical expressions most commonly used in eddy-current loss calculations are explained with equations in [6]. A significant segmentation of conductive massive parts may permit a significant reduction in the eddy-current losses [5,11–22]. The conductive material (such as magnets in electrical machines) can be segmented radially, axially, or circumferentially, depending on the direction of the applied magnetic field. In electrical machines, eddy-current loss reduction is particularly studied. However, in some cases, this result is not verified, and it is possible to generate an increase in volumic eddy-current losses with a low segmentation [17–19]. This phenomenon is called “anomaly of segmentation”. Eddy-current losses reach the maximum when the length of segmented material is nearly 2δ [18].

Despite the progress described above, very few researchers have developed methods to measure experimentally eddy-current losses. Furthermore, the measurements are always performed on rare-earth magnet materials with a spatially uniform applied magnetic field and compared to numerical results. In [23,24], the eddy-current losses of Nd-Fe-B sintered magnets were studied experimentally to determine the influence of segmentation. For this purpose, the magnet was inserted into a solenoid coil. The sinusoidal alternating magnetic field was generated by an alternating-current power supply. In [25], a study of higher frequencies and temperature effects under a (non-)sinusoidal applied magnetic field was performed. The excitation frequency was varied between 10 Hz and 1 kHz in [23], 1 kHz and 30 kHz in [24], and 50 Hz and 1 kHz (with a switching frequency of 8 kHz) in [25]. The eddy-current losses were calculated using

$$P_{ec} = c_p \cdot V_m \cdot \rho_v \cdot \frac{dT}{dt}, \quad (2)$$

where T is the measured temperature of the magnet, c_p is the specific heat capacity of the magnet, V_m is the volume of the magnet, and ρ_v is the volumetric mass density of the magnet. The transient phase when the temperature increases at the beginning of the experiment permits the estimation of the eddy-current losses. In [26], the same method was applied to a synchronous machine at frequencies of 133.3 Hz and 400 Hz. As stated previously, in [27], the segmentation influence on the eddy-current losses is studied for a frequency of 50 Hz, again using thermal measurements.

In [28–30], based on double U-shaped closed magnetic circuit test equipment, the eddy-current losses were calculated as

$$P_{ec} = V_m \cdot f \cdot \int H \cdot dB_{av}, \quad (3)$$

where H and B_{av} are the magnetic field strength of the sample surface and the average magnetic flux density inside the sample, respectively. In [29], a frequency range of between 30 Hz and 150 Hz and segmentation (up to 6 segments) in one axis were investigated; while [30] studied a frequency range of between 100 Hz and 3 kHz but without segmentation.

In [31], a figure-of-eight-shaped magnetic circuit with a mobile armature was used. The eddy-current losses were determined by the decomposition of the power components based on different experimental measurements with a frequency range of between 50 Hz and 600 Hz, but the segmentation influence was not considered. In [32], the same method was used for a magnet inserted in a solenoid, with a “high” frequency ($500 \text{ Hz} < f < 1.8 \text{ kHz}$), and the impact of the segmentation was studied. In [33], the eddy-current losses are measured from a C-shaped magnetic circuit for different materials (stainless steel, carbon fiber, copper, titanium alloy) with a “high” frequency ($500 \text{ Hz} < f < 1 \text{ kHz}$).

The eddy-current losses can be estimated from experimental measurement using: (i) the thermometric method [23–26], (ii) the iron loss formulation [28–30], or (iii) the loss segregation method [31–33]. The latter technique will be used in this paper.

1.2. Objectives of the Study of Volumic Eddy-Current Losses

In this paper, the analytical determination of volumic eddy-current losses in rectangular-shaped conductive massive parts is presented with experimental validations. Eddy currents as well as resulting volumic losses are generated by a sinusoidal spatially uniform applied magnetic field with $f = 50$ Hz. The time study could be performed at any frequency and waveform, but this is not within the scope of this paper. A U-shaped electromagnetic device with a flat mobile armature (or adjustable air gap) allows the deduction of the volumic eddy-current losses for a spatially uniform but also non-uniform applied magnetic field (depending on the position of the studied material). As a first step, a 2D numerical model under the FEMM software [34] is developed in order to extract the magnetic field applied to conductive massive parts. A numerical and experimental comparison of the magnetic field is then performed. In the second phase, an accurate eddy-current loss estimation in rectangular-shaped aluminium conductive massive parts is performed and compared with the experimental test results. Moreover, the segmentation effect in both directions (i.e., y - and z -axes) is investigated. It is interesting to note that the mean input data, represented by the applied magnetic field distribution, can be deduced by a (semi-)analytical model (e.g., Maxwell–Fourier method, magnetic equivalent circuit, etc.), by a numerical method, or by experimental measurements. In this paper, the experimental measurements of the applied magnetic field distribution will be used for eddy-current loss estimation.

The rest of this article is organized as follows. Section 2 describes the electromagnet generating the magnetic field (with the advantages compared to a Helmholtz coil) as well as the aluminium conductive massive parts. In Section 3, the instrumentation and the experimental measures of the magnetic field distribution applied on conductive massive parts are presented. Furthermore, in order to evaluate the effectiveness of the mean input data for the eddy-current loss model, a comparative analysis between the experimental measurements and the numerical results of the applied magnetic field distribution is discussed. Section 4 describes the mathematical development of the analytical model, based on the Maxwell–Fourier method, for accurate eddy-current loss prediction in conductive massive parts. The analytical results have been compared to experimental test results in order to evaluate the effectiveness of the eddy-current loss model. This introduces the power conservation method (i.e., Boucherot’s theorem) in order to decompose the different values of the power consumed by the electromagnet with and without the conductive massive parts. The influence of segmentation of the conductive massive part is revealed. The different segmentation variants are compared and, in some cases, are specifically discussed. Finally, the conclusion is drawn in Section 5.

It is interesting to note that the analytical model of eddy-current losses can be adapted to any electromagnetic device or system (e.g., for different types of rotating or linear electrical machines with magnets). Nevertheless, the major constraint is that the conductive massive part must be geometrically rectangular-shaped. The studied material, where the eddy-current losses are generated, can be of any material (e.g., aluminium, copper, brass, iron, magnets, etc.). The most important input is the applied magnetic field, which must be spatially uniform and temporally sinusoidal (e.g., the fundamental component of the magnetic field in electrical machines).

2. U-Shaped Electromagnetic Device and Conductive Massive Parts Description

2.1. Overall View

The magnetic field source is a U-shaped electromagnetic device with a flat mobile armature (or adjustable airgap), which is illustrated in Figure 1 with the rectangular-shaped aluminium conductive massive parts. The electromagnet is supplied with a sinusoidal instantaneous voltage v at $f = 50$ Hz. The ferromagnetic circuit is not saturated with the voltage levels used. Therefore, the instantaneous electrical current i , flowing through the coils will also be sinusoidal with a maximum amplitude of $I_{\max} = 4.5$ A. The characteristics of the electromagnet (viz., ferromagnetic circuit and coil) are shown in Figure 2 and given in Table 1.

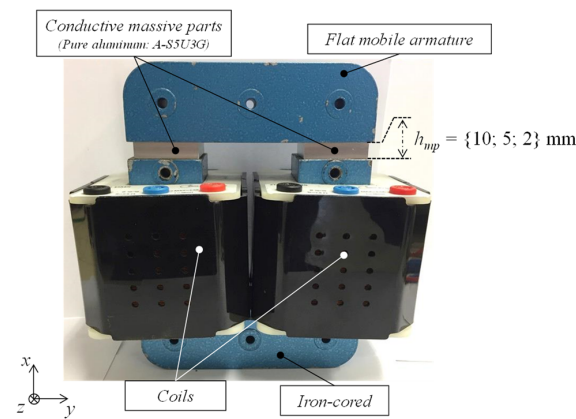


Figure 1. U-shaped electromagnetic device with a flat mobile armature (or adjustable airgap) with rectangular-shaped conductive massive parts.

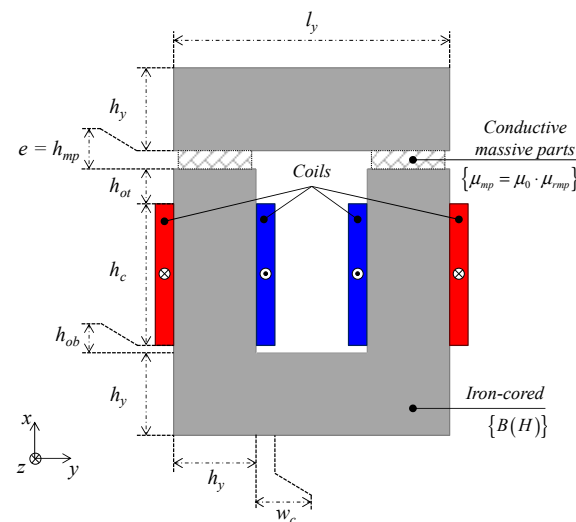


Figure 2. Electromagnet geometrical and physical parameters (legend: \otimes for the forward conductor and \odot for the return conductor).

Table 1. Parameters of the electromagnetic device.

	Symbol	Quantity	Values
Ferromagnetic circuit	d	Depth	46 mm
	w	Width	45 mm
	h_y	Yoke height	45 mm
	l_y	Yoke length	150 mm
	h_{ot}	Height overhang top	19 mm
	h_{ob}	Height overhang bot	4 mm
	μ_0	Vacuum permeability	$4\pi \cdot 10^{-7}$ H/m
	$B(H)$	FeSi ferromagnetic properties	Figure 3
Coils	N_t	Number of coils turns	500
	I_{max}	Maximal current (per coil)	4.5 A
	h_c	Coil height	77 mm
	w_c	Coil width	10 mm
	$S_c = w_c \times h_c$	Conductors area	700 mm^2
	r_c	Electrical resistance	2.8Ω
	L	Inductance	18 mH

One of the major advantages of the flat mobile armature electromagnet compared to a Helmholtz coil is that it is possible to modify the height of the air gap e in order:

- to have a more or less intense magnetic field in the air gap;
- to be able to insert conductive massive parts of various thicknesses h_{mp} ;
- and to displace the conductive massive parts with respect to the magnetic circuit to apply a spatially non-uniform applied magnetic field to the studied materials.

The values of $e = h_{mp}$ considered in this paper will be 10, 5, and 2 mm.

2.2. Ferromagnetic Circuit

The ferromagnetic circuit is composed of Iron Silicium (FeSi) sheets. Their magnetic properties are shown in Figure 3 (anhysteretic $B(H)$ and $\mu_r(B)$ curves).

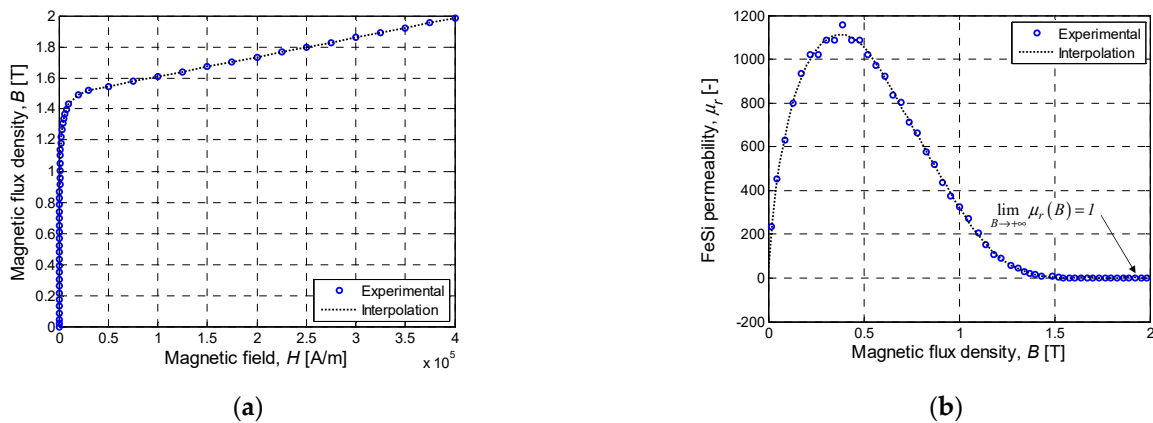


Figure 3. Characteristics of FeSi sheets: (a) Anhysteretic $B(H)$ curve, and (b) $\mu_r(B)$ curve.

2.3. Coils and Connections

Two identical coils, having N_t series of turns, are associated with the ferromagnetic circuit as shown in Figure 1. These coils create a magnetic flux linkage ψ in the iron core and the conductive massive parts. The coils' arrangement in the electromagnet allows for magnetic symmetry of fluxes (viz., principal and leakage flux). In order to obtain a maximum magnetic field in the air gap e and, consequently, to measure higher eddy-current losses, the coils must be connected in parallel as shown in Figure 4.

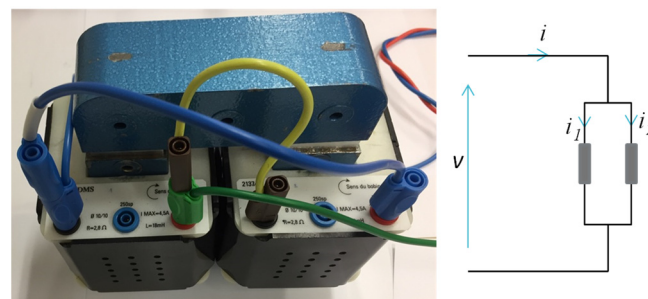


Figure 4. View of the connections and electrical scheme.

According to Faraday–Hopkinson law, we have

$$v = R \cdot i + \omega \cdot \frac{\partial \psi}{\partial \theta_{rs}} \text{ with } \theta_{rs} = \omega \cdot t, \tag{4}$$

$$\psi = \frac{N_t^2}{\mathfrak{R}} \cdot i = L_m \cdot i, \tag{5}$$

where $R = r_c/2$ is the total electrical resistance for a parallel coupling with r_c the electrical resistance of the coil, θ_{rs} is the electrical angular position, \Re is the principal magnetic reluctance, and L_m is the magnetizing inductance.

By assuming that the resistive part can be considered negligible compared to the inductive part, the root mean square (RMS) current I and the phase shift φ (between i and v) of i are determined by

$$I \cdot e^{j \cdot \varphi} \cong \frac{V}{j \cdot \omega \cdot L_m} = \frac{V}{\omega \cdot L_m} \angle -\pi/2 \quad (6)$$

where V is the RMS voltage.

It can be seen that for a given V , if the number of coil turns is increased, then the RMS current I as well as the generated magnetic field is less important. According to (6), the phase shift φ is approximately equal to $-\pi/2$.

2.4. Conductive Massive Parts

This experimental device allows the characterization of $N_{mp} = 2$ conductive massive parts at the same time, as illustrated in Figure 1. The flat mobile armature allows the height of the air gap e to be changed and conductive massive parts to be inserted. In our study, rectangular-shaped aluminium conductive massive parts (aluminium: A-S5U3G) have been considered with $\sigma_{mp} = \sigma_{Al} = 20 \times 10^6$ S/m.

The segmentation effect, which is also investigated in this paper, influences the eddy currents and, therefore, the eddy-current losses. In the yz -plane, the conductive massive part can be decomposed into $N_{s_z} \times N_{s_y}$ regular conductive segments in which $N_{s_y} \in \mathbb{N}^*$ and $N_{s_z} \in \mathbb{N}^*$ are, respectively, the segmentation number in the y -axis and the z -axis. The various segmentations $\{N_{s_z}, N_{s_y}\}$ are shown in Figure 5. Furthermore, it should be noted that the various conductive segments of a conductive massive part are glued together and isolated from each other. The pitch size of the isolation is 0.06 mm (type: Ruban Kapton).

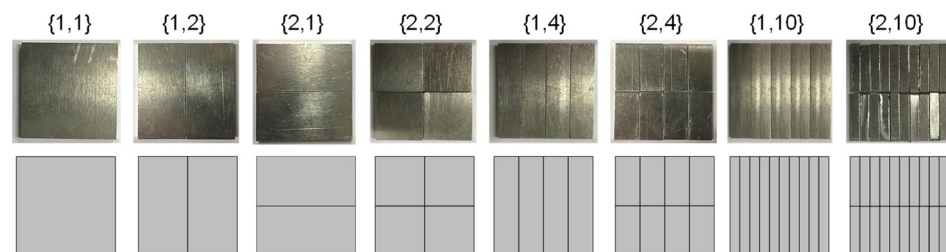


Figure 5. Description of segmentations $\{N_{s_z}, N_{s_y}\}, \forall h_{mp}$.

3. Applied Magnetic Field Distribution with Experimental Validations

In this section, the main objective is to precisely establish and measure the magnetic field distribution applied on the aluminium conductive massive parts generated by the electromagnet as a function of the current injected into the coils. The experimental measurements of this magnetic field will be the mean input data for the analytical model of eddy-current losses.

3.1. Instrumentation

3.1.1. Hall Effect Sensor

The value of the magnetic field in the air gap is obtained by using a Hall effect sensor HE144T (Asensor Technology AB[®] [35]). This sensor, with an estimated uncertainty of 1%, is shown in Figure 6a. One of the advantages of this sensor is its thickness, which is only 0.5 mm. This Hall effect sensor has four pins, two to supply the probe with a direct current of 1 mA, and two to measure the Hall voltage and recover the value of the measured magnetic field.

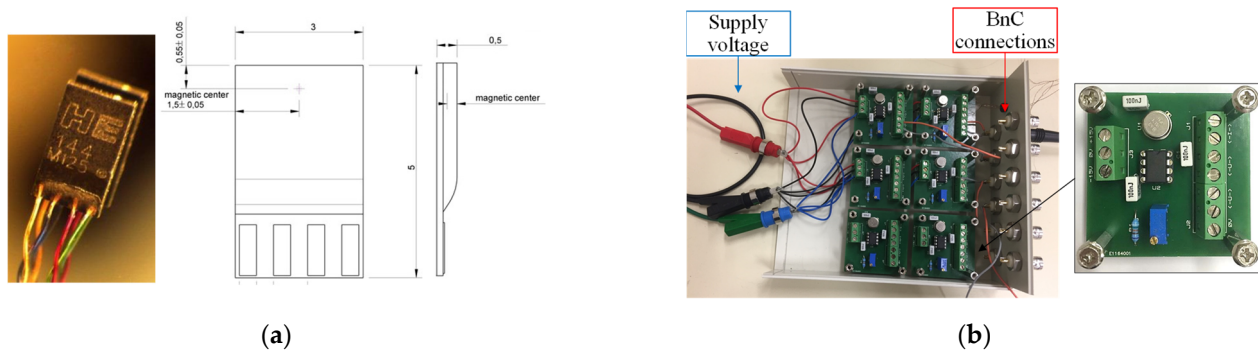


Figure 6. Instrumentation: (a) Hall effect sensor HE144T [35], and (b) Power/acquisition box.

In order to power a 1 mA probe, an electrical circuit diagram (supplied with $-15\text{ V}/0\text{ V}/15\text{ V}$) was created and developed with the Proteus Isis software (Version 8.2, Société Labcenter Electronics, France). Subsequently, EuroCircuits[®] was used to fabricate printed circuits (single track cards) onto which various components were soldered to obtain the final version presented in Figure 6b. In order to measure the magnetic field on a given path quickly and precisely, a total of 12 Hall effect sensors was determined to be the optimal and cost-effective choice. Figure 6b presents the created power/acquisition box, which can contain 12 printed circuits. In order to observe the magnetic field signals, the sensors' outputs are connected to the BNC cables, which can be directly connected to an oscilloscope.

3.1.2. Sensor Supports

Various supports have been realized to make it possible to measure the magnetic field very precisely at regular intervals, as shown in Figure 7. These supports (non-magnetic and non-conductive) are produced by 3D printing in PolyLactic Acid (PLA). The thickness of the measuring supports must be the same as the thickness of the conductive massive parts (viz., $e = h_{mp}$) so that the magnetic field in the air gap can be measured correctly for the eddy-current loss calculation.

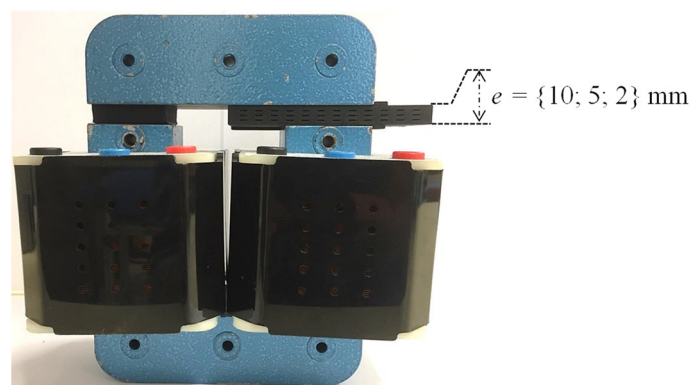


Figure 7. Sensor supports in the air gap e of the electromagnet.

Figure 8 presents the various supports and their arrangements according to the desired air-gap thickness. For $e = 10\text{ mm}$ (Figure 8a), it was possible to make three layers of 12 slots (i.e., 36 measurement locations). When $e = 5\text{ mm}$ (Figure 8b), the support is composed of two layers of 12 slots (i.e., 24 measurement locations). For the final support of $e = 2\text{ mm}$ (Figure 8c), the printing method was modified to solve the problem related to the thinness of the geometry, and only 12 measurements were possible.

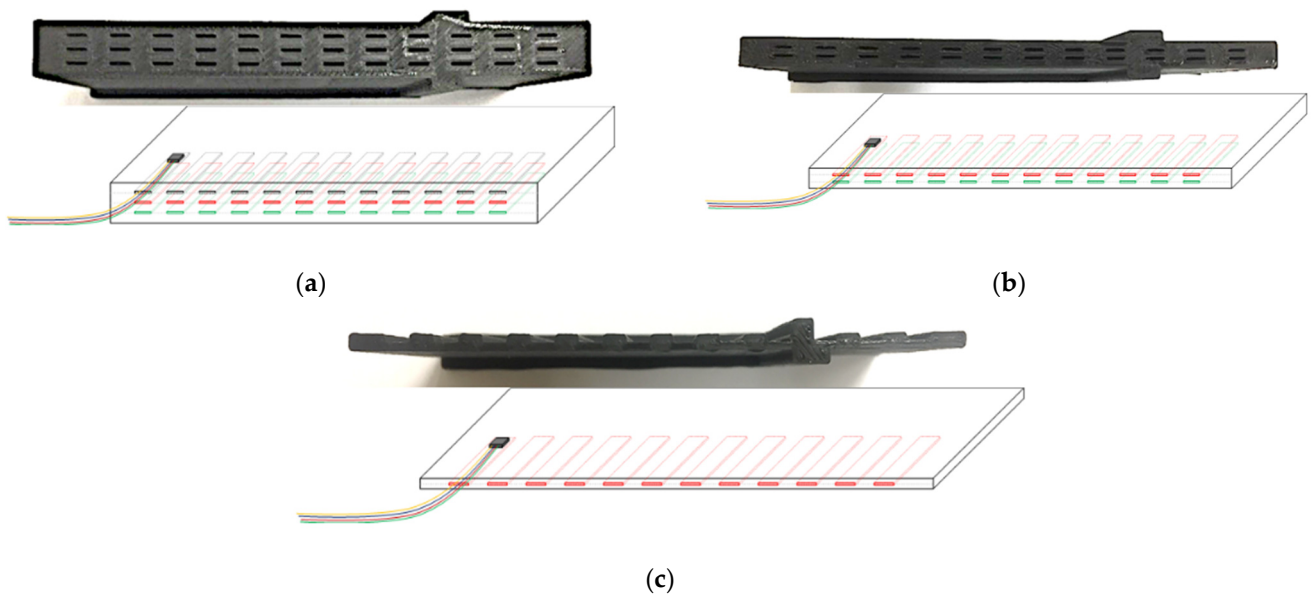


Figure 8. Sensor supports in PLA for the air gap $e =$: (a) 10 mm, (b) 5 mm, and (c) 2 mm.

3.2. Experimental Measurements

3.2.1. Temporal Evolutions of i , v , and h_{ox}

It is possible to visualize the temporal evolutions over an electrical period of the different quantities such as the current i , the voltage v , and the normal magnetic field at the sensor support h_{ox} . The measurements are realized for $I = 3$ A (viz., $V = 90$ V). The various temporal evolutions for a 10 mm air gap are shown in Figure 9.

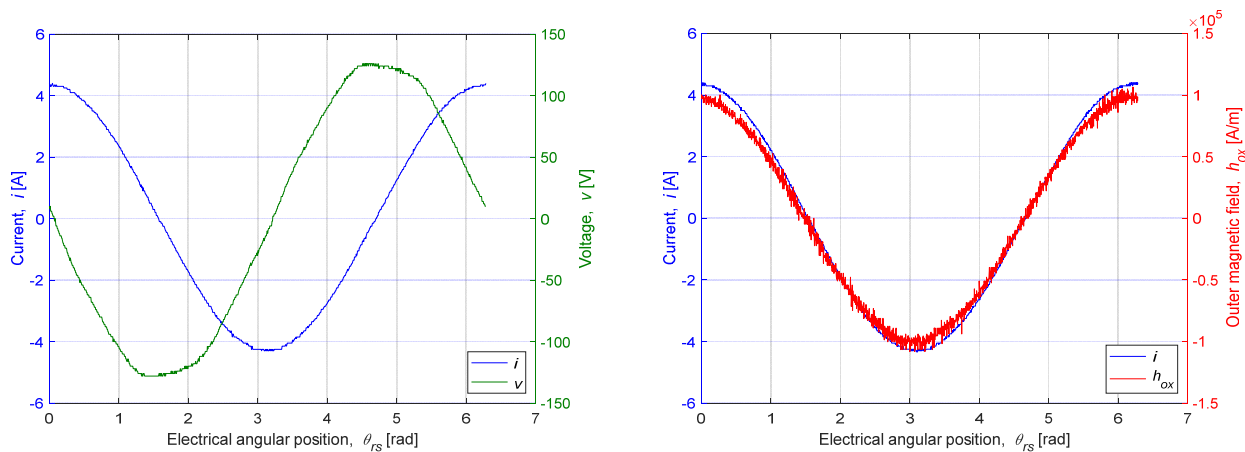


Figure 9. Temporal evolution over an electrical period of $i(\theta_{rs})$, $v(\theta_{rs})$, and $h_{ox}(\theta_{rs})$ in a 10 mm air gap with $I = 3$ A.

By comparing the various curves, some generalities could be made:

- i and v (only the fundamental components) have a phase shift φ of $\approx -\pi/2$ as demonstrated by (6);
- i and h_{ox} are still in phase.

3.2.2. Linear Dependency of $V(I)$ and $H_{ox}(I)$

The electromagnet is voltage-controlled, for an RMS voltage V varying from 0 to 230 V in 10 V steps, the RMS current I flowing in the coils is measured.

Figure 10 shows the dependence between V and I for the three air-gap thicknesses detailed previously. It can be seen that, for a given V , when e increases (equivalent to a

decrease in the magnetizing inductance L_m , I also increases. Moreover, V is proportional to I for the various thicknesses, and it could be deduced that the device does not saturate.

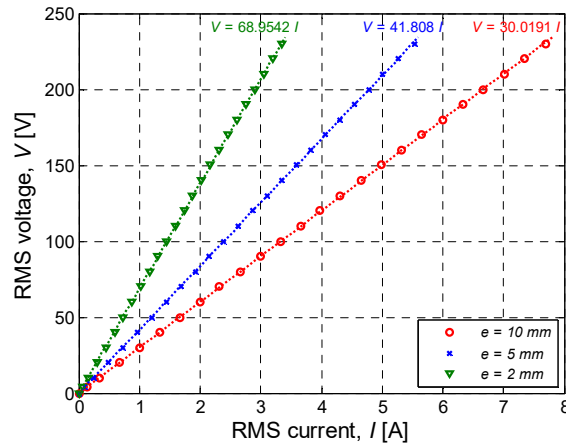


Figure 10. Linear dependency between V and I for each air-gap thickness.

Concerning the measured maximum magnetic field, H_{ox} , the measurements are performed in the middle of the air gap for the three air-gap thicknesses. Figure 11 shows the dependence between H_{ox} and I . It can be seen that, for a given I , when e increases, H_{ox} decreases. The generated maximum magnetic field H_{ox} is therefore the image of I . These conclusions are confirmed by (assuming that $\mu_r \rightarrow +\infty$)

$$H_{ox} \cong \frac{N_t \sqrt{2}}{2 \cdot e} \cdot I \text{ (resulting from Hopkinson's law)}. \tag{7}$$

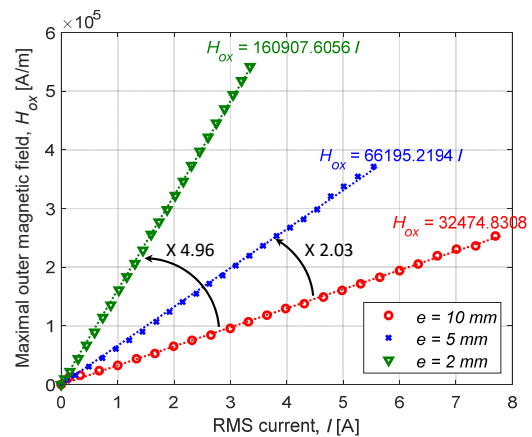


Figure 11. Linear dependency between H_{ox} (measured in the middle of the air gap) and I for each air-gap thickness.

It is interesting to note that the slopes, as well as the ratios between the various curves in Figure 11, can be validated by (7).

3.2.3. Spatial Evolution of H_{ox}

The study aims to determine the spatial distribution of the magnetic field generated in the air gap along the flux paths (or sensor support layers) (see Figure 8). Figure 12 presents the spatial distribution of the measured maximum magnetic field H_{ox} for a 10 mm air gap at the various layers (that is 36 measurement locations). The measurements are realized for $I = 3$ A (viz., $V = 90$ V). It can be observed that H_{ox} is homogeneous (or spatially uniform) throughout the air gap with a value close to 100 kA/m. Moreover, due to leakage fluxes, the

levels of H_{ox} are different at the edges (the right and the left sides of the air gap) and in the middle of the air gap. The magnetic leakages are more important inside the electromagnet than outside at the air gap and can be assumed to be negligible.

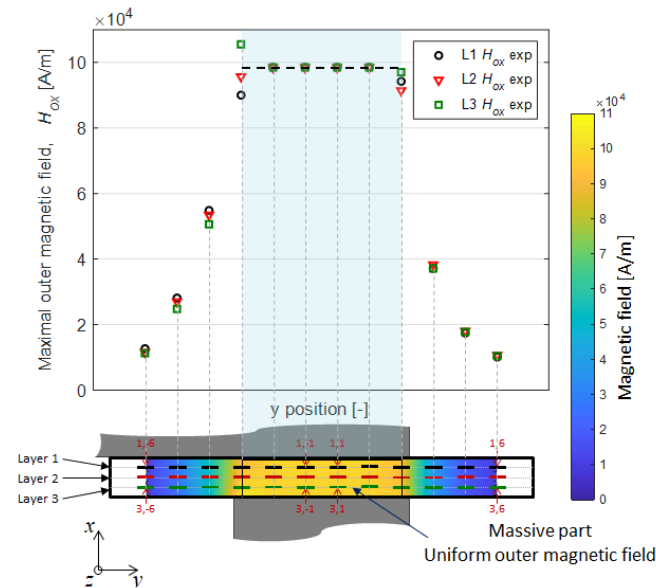


Figure 12. Spatial evolution of H_{ox} for the various layers in a 10 mm air gap with $I = 3$ A.

3.3. Comparison between Measurements and Numerical Results

The objective here is to perform a comparative analysis of the magnetic generated in the air gap (without the conductive massive parts) between the experimental measurements and the numerical results, in order to evaluate the effectiveness of the mean input data for the eddy-current loss model.

3.3.1. Numerical Modeling

The numerical model, under the FEMM software [34], considers the electromagnet without the conductive massive parts introduced previously (see Figures 2 and 7). A calculation code developed using the Matlab[®] environment allows us to execute commands in the FEMM software, as illustrated in Figure 13.

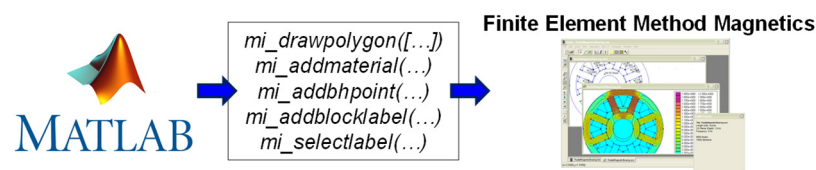


Figure 13. Schematic representation of the Matlab[®]–FEMM software interface.

The assumptions used in the static numerical model are:

- the model is supposed to be in 2D (i.e., the end effects are neglected);
- the magnetic materials are considered to be isotropic;
- the hysteresis effect is ignored;
- and the skin effect in all materials (e.g., copper and iron) is neglected.

The 2D numerical mesh (with 7463 nodes) of the electromagnet is illustrated in Figure 14. The numerical simulations are performed for the three air-gap thicknesses with $I = 3$ A (viz., $V = 90$ V) and by using the FeSi ferromagnetic properties (see Figure 3).

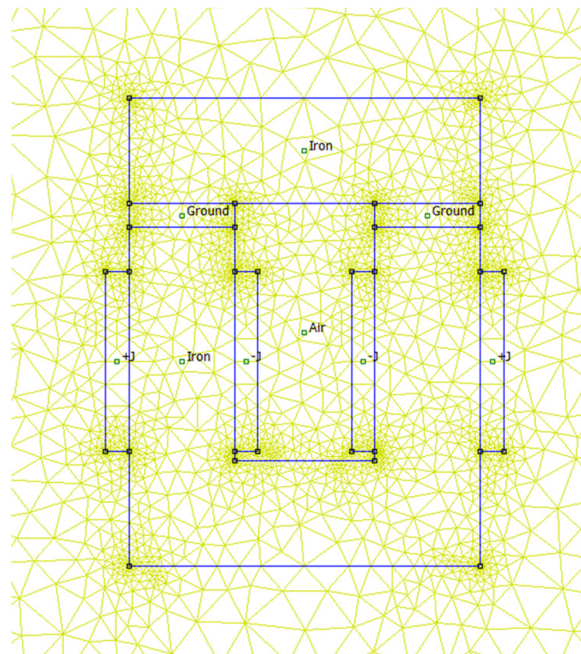
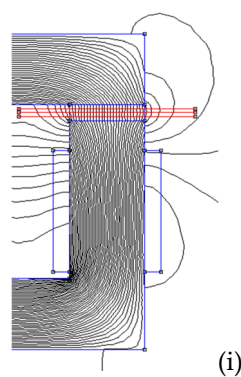


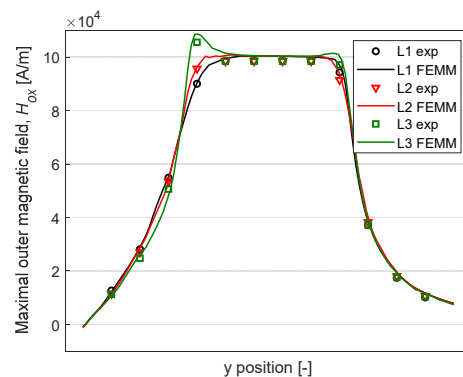
Figure 14. 2D numerical mesh of the electromagnetic device with a 10 mm air gap.

3.3.2. Results Discussion

Figure 15a presents the equipotential lines (≈ 90 lines) of the magnetic vector potential in the electromagnet with the 2D numerical modeling. The validation paths of the maximum magnetic field H_{ox} for the comparison are given in Figure 15a (equivalent to various layers in Figure 8). The spatial evolution of H_{ox} are represented on the various paths in Figure 15b. The solid lines represent H_{ox} computed by the 2D numerical modeling and the symbols correspond to experimental measurements. It can be seen that a very good agreement between the experimental measurements and the numerical results is obtained whatever the validation paths and the air-gap thickness. By observing the equipotential lines, it could be concluded that a decrease in the air-gap thickness reduces the leakage fluxes, and thus, a more uniform magnetic field is observable in the active part of the electromagnetic (such as the transition of Figure 15a(i) to Figure 15b(iii)). At the extremities, the magnetic field decreases faster.



(i)



(i)

Figure 15. Cont.

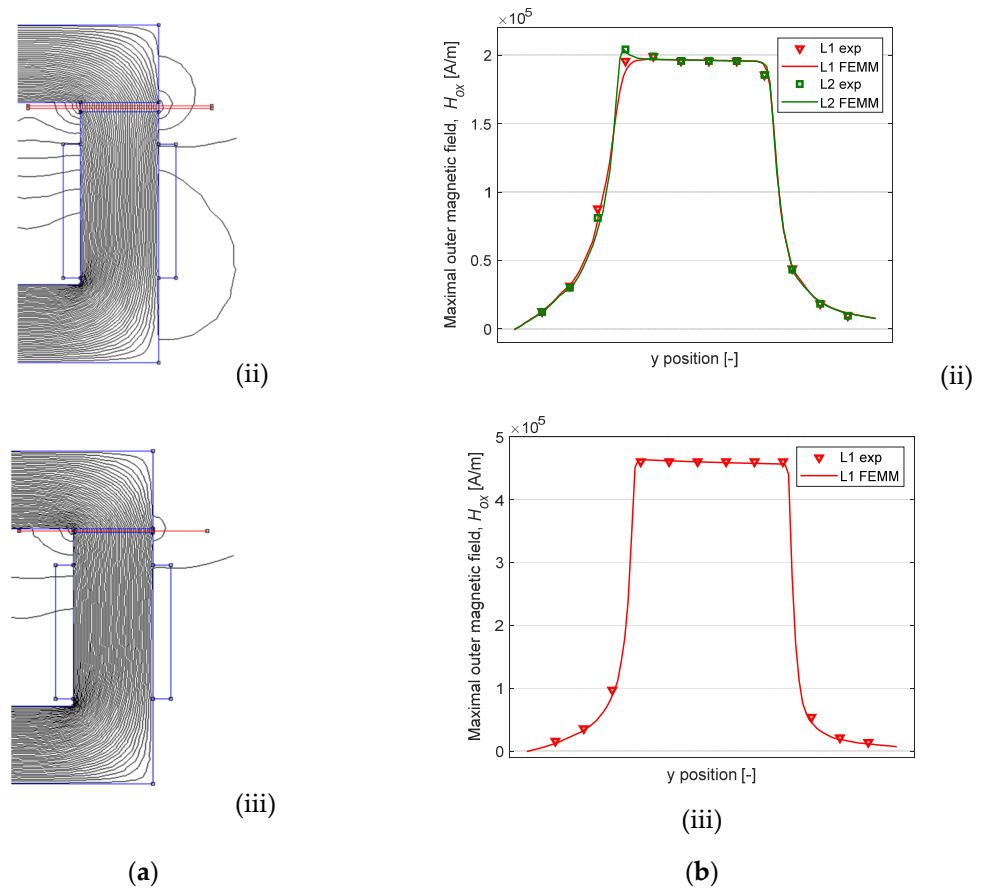


Figure 15. (a) Equipotential lines and (b) Experimental and numerical comparisons of H_{ox} with $I = 3$ A for the air gap $e =$: (i) 10 mm, (ii) 5 mm, and (iii) 2 mm.

The normal component H_{ox} and the module $|H_o|$ of the magnetic field in the air gap are plotted in Figure 16. The studied case is the following: a 10 mm air gap (maximum leakage), and an RMS current $I = 3$ A (viz., $V = 90$ V). By comparing the magnetic field values obtained from the numerical modeling, the similar evolutions of H_{ox} and $|H_o|$ could be observed for all the studied paths. This confirms that the normal component H_{ox} of the magnetic field is predominant. Eddy currents are induced only by the normal component H_{ox} and the effects of the tangential component H_{oy} on the eddy-current loss calculation can be neglected.

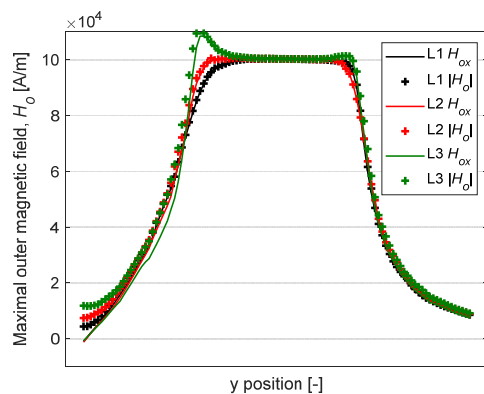


Figure 16. Numerical analysis of the magnetic field in the air gap (between the normal component H_{ox} and the module $|H_o|$) for a 10 mm air gap with $I = 3$ A.

4. Eddy-Current Loss Calculation with Experimental Validations

In this section, the main objective is to estimate analytically and experimentally the volumic eddy-current losses in rectangular-shaped aluminium conductive massive parts generated by a varying applied magnetic field (see Section 3).

4.1. Analytical Model

4.1.1. Introduction

The analytical model is based on the formal resolution of the magnetodynamic Maxwell’s equations in Cartesian coordinates (x, y, z) by using the separation of variables method and the Fourier series. By applying boundary conditions (BCs) to the edges of the conductive massive part, the inner (or resulting) magnetic field in the conductive massive parts considering the skin effect can be obtained analytically. From this quantity, the resultant eddy-current density distribution as well as the eddy-current losses can be determined analytically. These losses have been established from Poynting’s theorem. The segmentation effect in both directions (i.e., y -axis and z -axis) is also considered in the mathematical development of the analytical model.

4.1.2. Assumptions and Segmentation

Figure 17a represents the geometrical/physical parameters of the conductive massive part and the coordinate system used. The simplifying assumptions are:

- the studied materials are excited by a spatially uniform outer magnetic field supposed normal to the yz -plane, as shown in Figure 17a; i.e., $\mathbf{H}_{o\perp} = \{H_{o\perp}; 0; 0\}$ with $H_{o\perp} = H_{ox} = h_{ox} \cdot \mathbf{u}_x$ where \mathbf{u} is the unity vector of the three components;
- the eddy currents are induced only by h_{ox} and the effects of other magnetic field components on the eddy-current loss calculation can be neglected;
- the studied materials are rectangular-shaped only and considered to be isotropic (i.e., the magnetic permeability μ_{mp} and the electrical conductivity σ_{mp} of the conductive massive part are constant);
- and σ_{mp} is assumed to be invariant to the operating temperature.

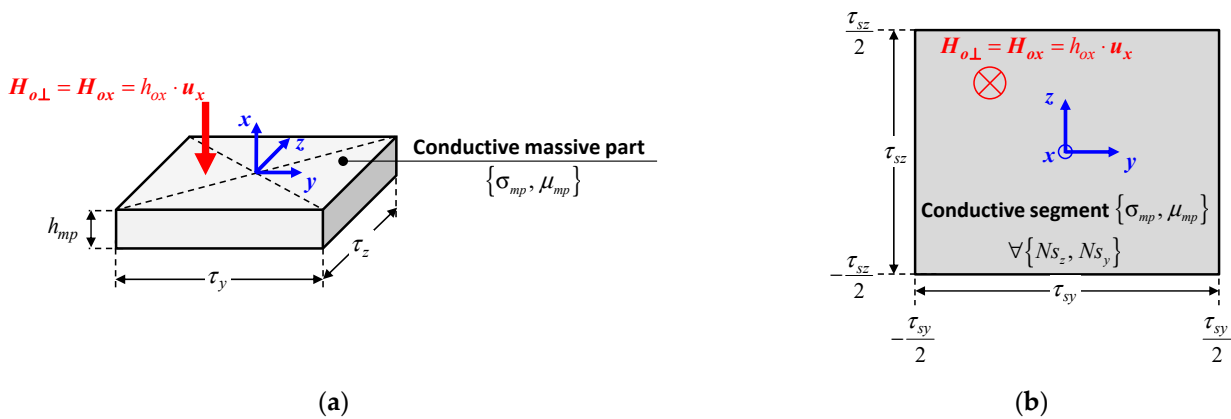


Figure 17. Geometrical/physical parameters and coordinate system: (a) general view, and (b) yz -plane of a conductive segment of the conductive massive part, $\nabla\{N_{s_z}, N_{s_y}\}$.

Regarding the last assumption, even if the temperature of the conductive massive part varies, the maximum increase ($<4\%$) of σ_{mp} (viz., $20 \times 10^6 < \sigma_{mp} < 20.8 \times 10^6$ S/m) will not have a significant influence on the eddy-current losses.

In Section 3, it was demonstrated that:

- the leakage fluxes at the edges of the conductive massive parts could be neglected (such as h_{ox} is independent of x , $\forall h_{mp}$);
- and the electromagnet supplied with a sinusoidal voltage was not saturated.
- Therefore, the analytical model can be developed in 2D and the yz -plane. Hence,

- the resultant eddy-current density has two components, i.e., $J_\sigma = \{0; J_{\sigma y}; J_{\sigma z}\}$ with $J_{\sigma y} = j_{\sigma y} \cdot \mathbf{u}_y$ and $J_{\sigma z} = j_{\sigma z} \cdot \mathbf{u}_z$;
- and the inner (or resulting) magnetic field in the conductive massive parts considering the skin effect $\mathbf{H}_i = \{H_{ix}; 0; 0\}$ with $H_{ix} = h_{ix} \cdot \mathbf{u}_x$.

In the unsaturated state, all electromagnetic quantities can be considered to be sinusoidal, i.e.,

$$q = \text{Re}\{Q \cdot e^{j \cdot \theta_{rs}}\} \text{ with } j = \sqrt{-1} \quad (8)$$

where Q is the maximum complex amplitude of q .

The segmentation effect influences the eddy currents, and therefore, the eddy-current losses. Figure 17b shows a conductive segment whose geometrical parameters are defined by

$$\tau_{sy} = \frac{\tau_y}{N_{s_y}} \text{ and } \tau_{sz} = \frac{\tau_z}{N_{s_z}}. \quad (9)$$

For $N_{s_z} \times N_{s_y} = 1 \times 1$, the conductive massive part is not segmented. In Section 3, it was observed that h_{ox} applied to the studied materials was homogeneous (or spatially uniform) over the whole piece. Therefore, the inner (or resulting) magnetic field h_{ix} , the distribution of J_σ , as well as the eddy-current losses, can be considered identical in each conductive segment, $\forall \{N_{s_z}, N_{s_y}\}$. It is interesting to note that this remark is no longer valid when h_{ox} is spatially non-uniform because the eddy-current losses would be more or less different in each conductive segment.

4.1.3. Resulting Magnetic Field

- **Governing Partial Differential Equation (PDE) in Cartesian Coordinate (y, z):** In the quasi-stationary approximation, inside a linear (non)magnetic material without electromagnetic sources, the magnetodynamic PDE in terms of h_{ix} , resulting from Maxwell's equations, is defined by

$$\nabla^2 h_{ix} - \mu_{mp} \cdot \sigma_{mp} \cdot \omega \cdot \frac{\partial h_{ix}}{\partial \theta_{rs}} = 0 \text{ (Diffusion equation)}. \quad (10)$$

Using (7), (9) becomes, in complex notation

$$\nabla^2 H_{ix} - \alpha_{mp}^2 \cdot H_{ix} = 0 \text{ (Helmholtz's equation)} \quad (11)$$

$$\alpha_{mp} = \sqrt{j \cdot \mu_{mp} \cdot \sigma_{mp} \cdot \omega} = \frac{1+j}{\delta_{mp}} \quad (12)$$

where δ_{mp} is the skin depth of the conductive massive part defined by (1), and $\nabla^2 H_{ix}$ is the complex Laplacian of h_{ix} in the yz -plane

$$\nabla^2 H_{ix} = \frac{\partial^2 H_{ix}}{\partial y^2} + \frac{\partial^2 H_{ix}}{\partial z^2}. \quad (13)$$

By using the separation of variables method, the 2D general solution of H_{ix} in both directions (i.e., y -axis and z -axis) can be defined by a complex Fourier series [1]. The unknown coefficients are determined analytically from the BCs at the edges of each conductive segment.

- **Definition of BCs:** Since the conductive massive parts are excited by an outer sinusoidal spatially uniform magnetic field, the BCs can be considered homogeneous [see Section 3] and equal to $-H_{ox}$ (according to the Cartesian coordinates of Figure 17) on the edges, $\forall \{N_{s_z}, N_{s_y}\}$:
 - in the y -axis:

$$h_{ix}\left(y, \pm \frac{\tau_{sz}}{2}, \theta_{rs}\right) = h_{ox} \Rightarrow H_{ix}\left(y, \pm \frac{\tau_{sz}}{2}\right) = -H_{ox}, \quad (14)$$

- in the z-axis:

$$h_{ix}\left(\pm \frac{\tau_{sy}}{2}, z, \theta_{rs}\right) = h_{ox} \Rightarrow H_{ix}\left(\pm \frac{\tau_{sy}}{2}, z\right) = -H_{ox}. \tag{15}$$

Nevertheless, it is interesting to note that imposing $-H_{ox}$ as a BC on the edges remains a more or less rigorous approximation (e.g., the negligible magnetic leakages, etc.).

➤ **Magnetic Field Solution:** By satisfying (14) and (15), the 2D final solution of H_{ix} (viz., the complex amplitude of h_{ix}) in each conductive segment can be written as a Fourier series

$$H_{ix} = -H_{ox} \cdot \left[\frac{\cosh(\alpha_{mp} \cdot z)}{\cosh(\alpha_{mp} \cdot \frac{\tau_{sz}}{2})} + \sum_n e_n \cdot \cosh(\lambda_n' \cdot y) \cdot \cosh(\lambda_n \cdot z) \right], \tag{16}$$

$$e_n = 2 \cdot \left(\frac{\alpha_{mp}}{\lambda_n'} \right)^2 \cdot \frac{\text{sinc}\left(\lambda_n \cdot \frac{\tau_{sz}}{2}\right)}{\cosh\left(\lambda_n' \cdot \frac{\tau_{sy}}{2}\right)} \text{ with } \lambda_n' = \sqrt{\alpha_{mp}^2 + \lambda_n^2}, \tag{17}$$

where $\lambda_n = n \cdot \pi / \tau_{sz}$ is the spatial frequency (or periodicity) of H_{ix} with $n \in \{\mathbb{N}^*, N_{\max} | \text{odd}\}$ the spatial harmonic orders in which N_{\max} is the finite number of spatial harmonics terms.

4.1.4. Resultant Eddy-Current Density Distribution

According to the superposition principle, the magnetic field due to eddy currents $H_\sigma = \{H_{\sigma x}; 0; 0\}$ with $H_{\sigma x} = h_{\sigma x} \cdot u_x$ is defined by

$$h_{\sigma x} = h_{ix} - h_{ox} \Rightarrow H_{\sigma x} = H_{ix} - H_{ox}. \tag{18}$$

From the Maxwell–Ampère law (i.e., $J_\sigma = \nabla \times H_\sigma$), the complex amplitudes of $j_{\sigma y}$ and $j_{\sigma z}$ in each conductive segment are respectively given by

$$J_{\sigma y} = H_{ox} \cdot \left[\alpha_{mp} \cdot \frac{\sinh(\alpha_{mp} \cdot z)}{\cosh(\alpha_{mp} \cdot \frac{\tau_{sz}}{2})} - \sum_n e_n \cdot \lambda_n \cdot \cosh(\lambda_n' \cdot y) \cdot \sin(\lambda_n \cdot z) \right], \tag{19}$$

$$J_{\sigma z} = H_{ox} \cdot \sum_n e_n \cdot \lambda_n' \cdot \sinh(\lambda_n' \cdot y) \cdot \cos(\lambda_n \cdot z). \tag{20}$$

4.1.5. Volumic Eddy-Current Losses

The complex time-averaged Poynting vector over time in each conductive segment is defined by

$$\langle \Pi_{cs} \rangle = \frac{1}{2 \cdot \sigma_{mp}} \cdot (J_\sigma \times \overline{H}_i) = \frac{1}{2 \cdot \sigma_{mp}} \cdot \begin{pmatrix} 0 \\ J_{\sigma z} \cdot \overline{H}_{ix} \\ -J_{\sigma y} \cdot \overline{H}_{ix} \end{pmatrix}. \tag{21}$$

According to Poynting’s theorem, $\langle \Pi_{cs} \rangle$ across a closed surface S is given by the complex Poynting vector flux through this surface. From (14), (15) and (21), we obtain

$$\langle \Pi_{cs} \rangle = \iint_S \langle \Pi_{cs} \rangle \cdot dS = \frac{h_{mp}}{\sigma_{mp}} \cdot \left[\int_{-\frac{\tau_{sz}}{2}}^{\frac{\tau_{sz}}{2}} (J_{\sigma z} \cdot \overline{H}_{ix})_{y=-\frac{\tau_{sy}}{2}} \cdot dz - \int_{-\frac{\tau_{sy}}{2}}^{\frac{\tau_{sy}}{2}} (J_{\sigma y} \cdot \overline{H}_{ix})_{z=\frac{\tau_{sz}}{2}} \cdot dy \right]. \tag{22}$$

After the development, by substituting (16), (17), (19) and (20) into (22), the time-averaged apparent power in each conductive segment is then given by, $\forall \{N_{sz}, N_{sy}\}$,

$$\langle \Pi_{cs} \rangle = P_{cs} + j \cdot Q_{cs} = 2 \cdot \frac{h_{mp} \cdot |H_{ox}|^2}{\sigma_{mp}} \cdot \left(g_0 + \sum_n g_n \right), \tag{23}$$

$$g_0 = \alpha_{mp} \cdot \frac{\tau_{sy}}{2} \cdot \frac{\sinh\left(\alpha_{mp} \cdot \frac{\tau_{sz}}{2}\right)}{\cosh\left(\alpha_{mp} \cdot \frac{\tau_{sz}}{2}\right)}, \tag{24}$$

$$g_n = \frac{2}{\frac{\tau_{sz}}{2}} \cdot \frac{\lambda_n'}{\lambda_n^2} \cdot \left(\frac{\alpha_{mp}}{\lambda_n'}\right)^4 \cdot \frac{\sinh\left(\lambda_n' \cdot \frac{\tau_{sy}}{2}\right)}{\cosh\left(\lambda_n' \cdot \frac{\tau_{sy}}{2}\right)}, \tag{25}$$

where $P_{cs} = \text{Re}\{\langle \Pi_{cs} \rangle\}$ and $Q_{cs} = \text{Im}\{\langle \Pi_{cs} \rangle\}$ are the active and reactive power for each conductive segment, respectively.

It is interesting to note that the time-averaged apparent power in the rectangular-shaped conductive massive parts is calculated by

$$\langle \Pi_{mp} \rangle = N_{mp} \cdot N_{sz} \cdot N_{sy} \cdot \langle \Pi_{cs} \rangle = P_{mp} + j \cdot Q_{mp}. \tag{26}$$

where N_{mp} is the number of studied materials within the electromagnet.

4.2. Experimental Validations

4.2.1. Power Conservation Method

The process used to experimentally determine the eddy-current losses is the power conservation method. Firstly, the experimental measures must allow the characterization of the electromagnet in terms of power consumption. The various types of power measured are:

- P_{em} : the power consumed only by the electromagnet (i.e., without the studied materials);
- and, P_{tot} : the total power consumed by the electromagnet associated with the conductive massive parts.

In order to carry out compliant measurements of the power, it is necessary to respect

$$\oint_C H \cdot dl = \sum N_t \cdot i \text{ (Ampère's theorem)} \tag{27}$$

to keep the circulation length of the main magnetic flux with and without the conductive massive parts (see Figure 18). The studied materials are replaced by PLA. These supports (non-magnetic and non-conductive) are produced by 3D printing (see Section 3). According to (27), the PLA thickness should be equal to the height of conductive massive parts, as shown in Figure 18.



Figure 18. Electromagnet’s characterization in terms of power & validation of Ampère’s theorem: (a) P_{em} —Electromagnet power consumption, (b) P_{tot} —Total power.

Finally, from these data, the volumic eddy-current losses in the conductive massive parts can be deduced from

$$P_{mp} = P_{tot} - P_{em} \text{ (Boucherot's theorem)}. \tag{28}$$

It is interesting to note that the electromagnet is voltage-controlled, for an RMS voltage V varying from 0 to 230 V with 10 V steps, the RMS current I flowing in the coils is measured. Therefore, P_{em} and P_{tot} were measured for the same values of I and for the three air-gap thicknesses. The measurements are realized with a MetraHit 29S wattmeter.

4.2.2. Power Experimental Measurements

➤ **Electromagnet Power Consumption:** First, the electromagnetic device alone is characterized (see Figure 18a). The active power P_{em} (without the conductive massive parts replaced by PLA) is then measured.

In Section 3 (see Figure 11), it was demonstrated that H_{ox} in the conductive massive parts was the image of I . Hence, as an example, Figure 19 permits the visualization of P_{em} according to the squared RMS current I^2 and also the squared maximal outer magnetic field H_{ox}^2 for a 10 mm air gap. It can be observed that P_{em} is proportional to I^2 and H_{ox}^2 , $\forall e$. Moreover, from (7), for a given I^2 , P_{em} increases when e decreases. A power limitation due to the power supply can also be observed.

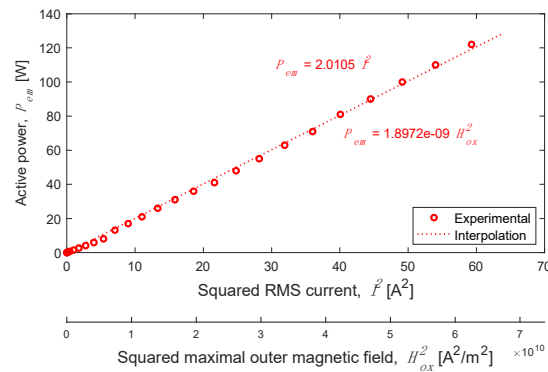


Figure 19. Linear dependency between P_{em} and I^2 or H_{ox}^2 for a 10 mm air gap.

➤ **Total Power:** Secondly, the conductive massive parts with(out) segmentation are introduced into the adjustable air gap. The total active power P_{tot} consumed by the electromagnet associated with the conductive massive parts (see Figure 18b) is then measured.

As an example, Figure 20 shows P_{tot} according to I^2 and H_{ox}^2 for conductive massive parts of 10 mm thickness and the various segmentations $\{N_{sz}, N_{sy}\}$ (Figure 5). It can be observed that P_{tot} is also proportional to I^2 and H_{ox}^2 , $\forall h_{mp}$. For a given I^2 , P_{tot} is less important for high thickness, $\forall \{N_{sz}, N_{sy}\}$. It is interesting to note that P_{tot} decreases with the increase in the number of conductive segments in conductive massive parts, $\forall h_{mp}$.

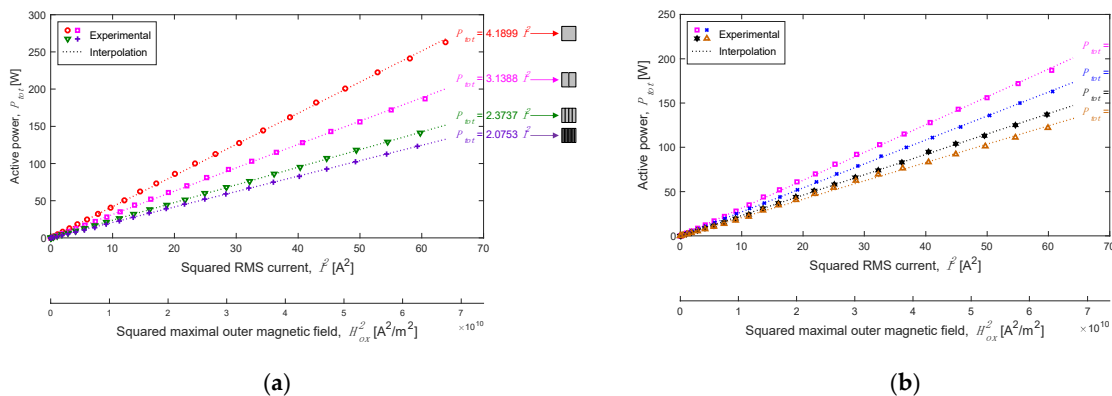


Figure 20. Linear dependency between P_{tot} and I^2 or H_{ox}^2 with $h_{mp} = 10$ mm for the segmentations $\{N_{sz}, N_{sy}\}$ where $N_{sy} = \{1, 2, 4, 10\}$ and: (a) $N_{sz} = 1$, and (b) $N_{sz} = 2$.

4.2.3. Analytical and Experimental Comparison of Volumic Eddy-Current Losses

➤ **Linear Dependency:** Knowing P_{em} and P_{tot} , the volumic eddy-current losses in conductive massive parts P_{mp} are determined from (26).

As an example, Figure 21 shows P_{mp} according to I^2 and H_{ox}^2 for conductive massive parts of 10 mm thickness and for the various segmentations $\{N_{sz}, N_{sy}\}$ (see Figure 5). The analytical results are in good agreement with the experimental measurements with a maximum error of less than 5%. The difference between the analytical and experimental results can be linked to $\forall h_{mp}$:

- the experimental method;
- and the variation of σ_{mp} due to the heating of the conductive massive parts (which is assumed to be invariant to the operating temperature in the analytical model).

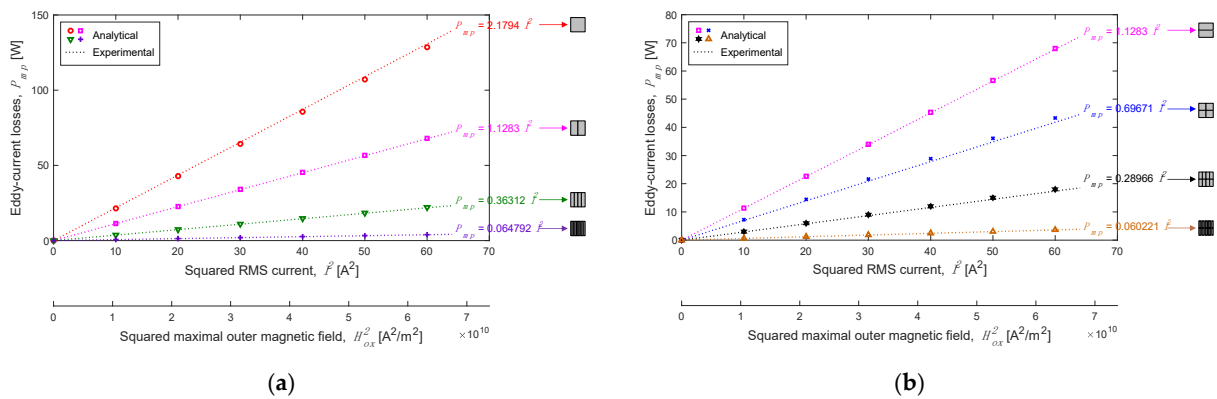


Figure 21. Linear dependency between P_{mp} and I^2 or H_{ox}^2 with $h_{mp} = 10$ mm for the segmentations $\{N_{sz}, N_{sy}\}$ where $N_{sy} = \{1, 2, 4, 10\}$ and: (a) $N_{sz} = 1$, and (b) $N_{sz} = 2$.

It can be observed that P_{mp} are proportional to I^2 and H_{ox}^2 , $\forall h_{mp}$. This can be explained by (23), (24) and (25). Under the applied conditions, for a sinusoidal spatially uniform applied magnetic field with $f = 50$ Hz, when the conductive massive parts are segmented, P_{mp} decrease, $\forall h_{mp}$. By inserting (7) into (23), (24) and (25), it is interesting to note that P_{mp} is inversely proportional to h_{mp} , $\forall \{N_{sz}, N_{sy}\}$.

➤ **Coefficient of Length/Skin Depth Study:** For this comparison analysis, $I = 3$ A (viz., $V = 90$ V). In order to study the segmentation influence on volumic eddy-current losses, they were plotted in relation to the coefficient of length/skin depth in both directions (such as τ_y/δ_{mp} in the y -axis and τ_z/δ_{mp} in the z -axis). In our study, the skin depth $\delta_{mp} = 16$ mm.

Figure 22 shows P_{mp} according to τ_y/δ_{mp} and τ_z/δ_{mp} for the various segmentations $\{N_{sz}, N_{sy}\}$ (Figure 5) and every thickness. The analytical results compared to the experimental measurements are consistent with a maximum error of less than 5% (viz., 4.67% for 4.67 W of difference for $P_{mp} = 95$ W with $\{1, 1\}$ and $h_{mp} = 2$ mm). Table 2 presents the various segmentations $\{N_{sz}, N_{sy}\}$ following the cross-section of a conductive segment S_{cs} , the perimeter of a conductive segment L_{cs} , τ_y/δ_{mp} , and τ_z/δ_{mp} . Firstly, it is interesting to note that P_{mp} is the same for $\{1, 2\}$ and $\{2, 1\}$, $\forall h_{mp}$. Secondly, P_{mp} decreases considerably when the ratios τ_y/δ_{mp} and/or τ_z/δ_{mp} are reduced, e.g., a loss reduction = $\approx 50\%$ when τ_y/δ_{mp} and/or τ_z/δ_{mp} is divided by 2: $\{1, 2\}$, $\{2, 1\}$ and $\{2, 2\}$ compared to $\{1, 1\}$, $\forall h_{mp}$. It can also be seen that for a segmentation > 4 in the y -axis, the segmentation into 2 in the z -axis has an insignificant influence on the loss reduction (viz., P_{mp} for $\{1, 4\} \neq P_{mp}$ for $\{4, 2\}$ and P_{mp} for $\{1, 10\} \cong P_{mp}$ for $\{2, 10\}$). Thirdly, for $\{1, 4\}$ and $\{2, 2\}$, it could be observed that S_{cs} is identical, however, P_{mp} is different (viz., P_{mp} for $\{1, 4\} < P_{mp}$ for $\{2, 2\}$). The segmentation $\{1, 4\}$ is more efficient since it presents a ratio $\tau_y/\delta_{mp} = 0.628$, while the segmentation $\{2, 2\}$ has a ratio $\tau_y/\delta_{mp} = 1.257$, $\forall h_{mp}$.

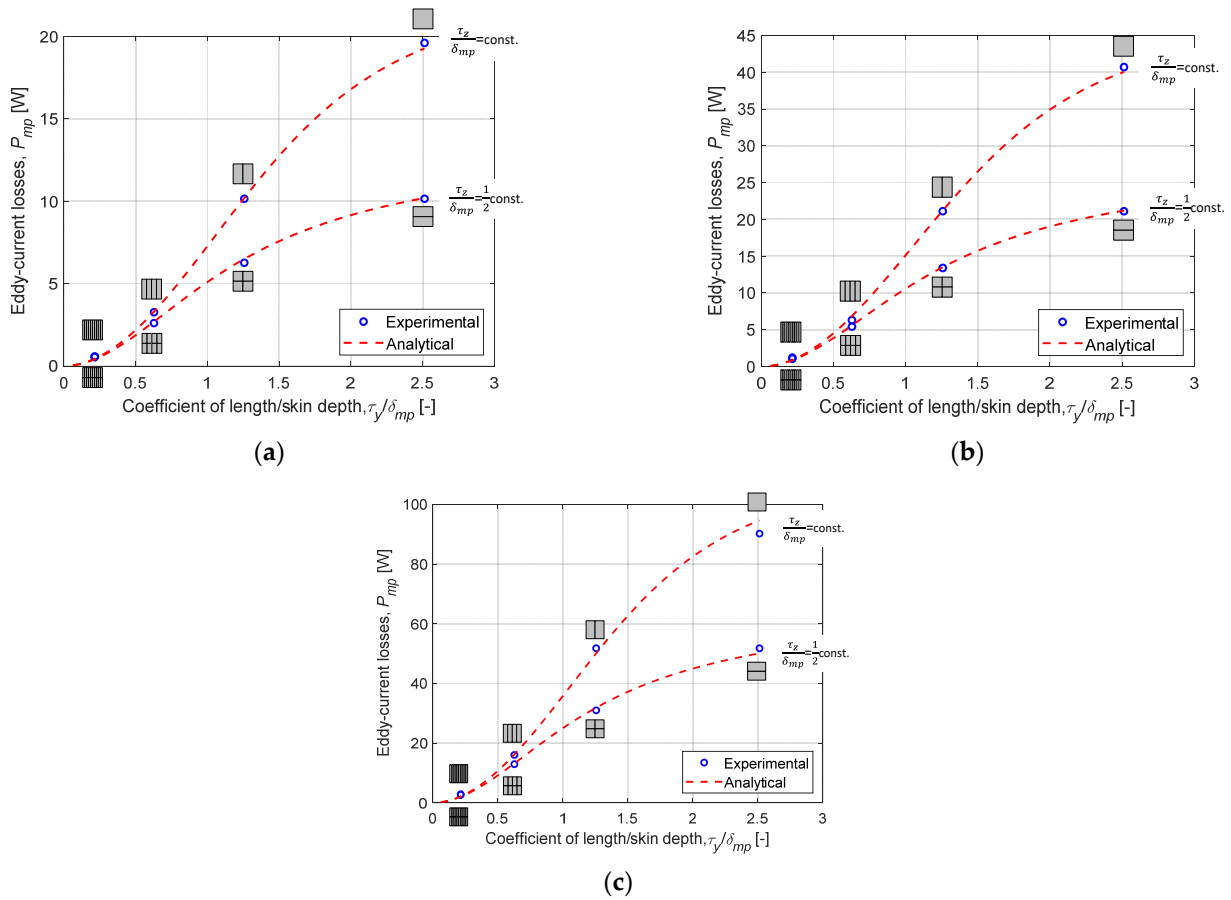


Figure 22. Volumic eddy-current losses P_{mp} vs. τ_y/δ_{mp} and τ_z/δ_{mp} with $I = 3$ A for $h_{mp} =$: (a) 10 mm, (b) 5 mm, and (c) 2 mm.

Table 2. Various segmentations in both directions vs. cross-section and perimeter of a conductive segment and coefficient of length/skin depth.

$\{Ns_z, Ns_y\}$		S_{cs} (mm ²)	L_{cs} (mm)	τ_y/δ_{mp}	τ_z/δ_{mp}
{1,1}		1600	160	2.513	2.513
{1,2}		800	120	1.257	2.513
{1,4}		400	100	0.628	2.513
{1,10}		160	88	0.251	2.513
{2,1}		800	120	2.513	1.257
{2,2}		400	80	1.257	1.257
{2,4}		200	60	0.628	1.257
{2,10}		80	48	0.251	1.257

5. Conclusions

This paper conducts an electromagnetic analysis of the magnetic field generated by a U-shaped electromagnetic device with a flat mobile armature (or adjustable air gap) and a volumic eddy-current loss estimation in conductive massive parts.

The experimental device was presented in detail. It includes an electromagnet, aluminium conductive massive parts (aluminium: A-S5U3G) with(out) segmentation, and its

instrumentation. The study on conductive massive parts was performed with a sinusoidal spatially uniform applied magnetic field at an excitation frequency of 50 Hz.

The spatial distribution of the magnetic field predicted by a 2D numerical model, under the FEMM software, has been compared to the experimental measurements. A good agreement between the experimental measurements and the numerical results has been achieved, with a mean percentage error (MPE) of less than 3%.

The accurate determination of the applied magnetic field has allowed an accurate eddy-current loss estimation in massive conductive parts. The losses were estimated from an analytical model, based on the Maxwell–Fourier method, and measured experimentally on (non-)segmented conductive massive parts. The analytically predicted eddy-current losses have been compared to the experimental results. The segmentation influence in both directions was studied. The comparison between the analytical and the experimental results allow the good accuracy to be confirmed. The maximal difference between experimental and analytical results is about 5 %, while the MPE is less than 2%.

Other frequencies (up to 600 Hz), time waveforms (e.g., six-step commutation, pulse-width modulation, etc.), geometrical shapes and materials (e.g., copper, brass, magnets, etc.) with different electrical conductivities [36] are a prospect for future study in order to explore the influence of segmentation further. Other prospects for future study are: (i) the volumic eddy-current loss distribution with a spatially non-uniform applied magnetic field, and (ii) the analytical and experimental validation of the eddy-currents reactance in conductive massive parts.

Author Contributions: Conceptualization, F.D.; methodology, A.P.; validation, A.P. and F.D.; writing—original draft preparation, A.P.; writing—review and editing, F.D.; supervision, F.D.; project administration, F.D. All authors have read and agreed to the published version of the manuscript.

Funding: This work was supported by RENAULT-SAS, Guyancourt, France. This scientific study is related to the project “Conception optimale des chaînes de Traction Electrique” (COCTEL) financed by the “Agence de l’Environnement et de la Maîtrise de l’Energie” (ADEME) under the program “Véhicule du futur des Investissements de l’avenir”.

Conflicts of Interest: The authors declare no conflict of interest.

References

1. Stoll, R.L. *The Analysis of Eddy Currents*; Clarendon Press: Oxford, UK, 1974.
2. Sikora, R.; Purczynski, J.; Lipinski, W.; Gramz, M. Use of variational methods to the eddy current calculation in thin conducting plates. *IEEE Trans. Magn.* **1978**, *14*, 383–385. [\[CrossRef\]](#)
3. Dresner, L. Eddy current heating of irregularly shaped plates by slow ramped fields. *OAK Ridge Natl. Lab. (ORNL)* **1978**, *6968*, 1–44.
4. Vansompel, H.; Yarantseva, A.; Sergeant, P.; Crevecoeur, G. An inverse thermal modeling approach for thermal parameter and loss identification in an axial flux permanent magnet machine. *IEEE Trans. Ind. Electron.* **2019**, *66*, 1727–1735. [\[CrossRef\]](#)
5. Benlamine, R.; Dubas, F.; Randi, S.A.; Lhotellier, D.; Espanet, C. 3-D numerical hybrid method for PM eddy-current losses calculation: Application to axial-flux PMSMs. *IEEE Trans. Magn.* **2015**, *51*, 8106110. [\[CrossRef\]](#)
6. Jassal, A.; Polinder, H.; Ferreira, J.A. Literature survey of eddy-current loss analysis in rotating electrical machines. *IET Electr. Power Appl.* **2012**, *6*, 743–752. [\[CrossRef\]](#)
7. Dubas, F.; Rahideh, A. Two-dimensional analytical permanent-magnet eddy-current loss calculations in slotless PMSM equipped with surface-inset magnets. *IEEE Trans. Magn.* **2014**, *50*, 6300320. [\[CrossRef\]](#)
8. Tessarolo, A. A survey of state-of-the-art methods to compute rotor eddy-current losses in synchronous permanent magnet machines. In Proceedings of the IEEE Workshop on Electrical Machines Design, Control and Diagnosis (WEMDCD), Nottingham, UK, 20–21 April 2017. [\[CrossRef\]](#)
9. Ouamara, D.; Dubas, F. Permanent-magnet eddy-current losses: A global revision of calculation and analysis. *Math. Comput. Appl.* **2019**, *24*, 67. [\[CrossRef\]](#)
10. Sirimanna, S.; Balachandran, T.; Haran, K.A. Review on magnet loss analysis, validation, design considerations, and reduction strategies in permanent magnet synchronous motors. *Energies* **2022**, *15*, 6116. [\[CrossRef\]](#)
11. Jara, W.; Lindh, P.; Tapia, J.A.; Petrov, I.; Repo, A.K.; Pyrhönen, J. Rotor eddy-current losses reduction in an axial flux permanent-magnet machine. *IEEE Trans. Ind. Electron.* **2016**, *63*, 4729–4737. [\[CrossRef\]](#)
12. De Paula Machado Bazzo, T.; Kölzer, J.F.; Carlson, R.; Wurtz, F.; Gerbaud, L. Multiphysics design optimization of a permanent magnet synchronous generator. *IEEE Trans. Ind. Electron.* **2017**, *64*, 9815–9823. [\[CrossRef\]](#)

13. Zheng, J.; Zhao, W.; Ji, J.; Zhu, J.; Gu, C.; Zhu, S. Design to reduce rotor losses in fault-tolerant permanent-magnet machines. *IEEE Trans. Ind. Electron.* **2018**, *65*, 8476–8487. [[CrossRef](#)]
14. Zhu, S.; Hu, Y.; Liu, C.; Wang, K. Iron loss and efficiency analysis of interior PM machines for electric vehicle applications. *IEEE Trans. Ind. Electron.* **2018**, *65*, 114–123. [[CrossRef](#)]
15. Martinek, G.; Lanz, M.; Schneider, G.; Goll, D. Determination of AC losses in segmented rare earth permanent magnets. *J. Appl. Phys.* **2020**, *128*, 113902. [[CrossRef](#)]
16. Amara, Y.; Wang, J.; Howe, D. Analytical prediction of eddy-current loss in modular tubular permanent-magnet machines. *IEEE Trans. Energy Convers.* **2005**, *20*, 761–770. [[CrossRef](#)]
17. Yamazaki, K.; Abe, A. Loss investigation of interior permanent-magnet motors considering carrier harmonics and magnet eddy currents. *IEEE Trans. Ind. Appl.* **2009**, *45*, 659–665. [[CrossRef](#)]
18. Huang, W.; Bettayeb, A.; Kaczmarek, R.; Vannier, J. Optimization of magnet segmentation for reduction of eddy-current losses in permanent magnet synchronous machine. *IEEE Trans. Energy Convers.* **2010**, *25*, 381–387. [[CrossRef](#)]
19. Mirzaei, M.; Binder, A.; Funieru, B.; Susic, M. Analytical calculations of induced eddy currents losses in the magnets of surface mounted PM machines with consideration of circumferential and axial segmentation effects. *IEEE Trans. Magn.* **2012**, *48*, 4831–4841. [[CrossRef](#)]
20. Mirzaei, M.; Binder, A.; Deak, C. 3D analysis of circumferential and axial segmentation effect on magnet eddy-current losses in permanent magnet synchronous machines with concentrated windings. In Proceedings of the XIX International Conference on Electrical Machines—ICEM 2010, Rome, Italy, 6–8 September 2010. [[CrossRef](#)]
21. Balamurali, A.; Lai, C.; Mollaeian, A.; Loukanov, V.; Kar, N.C. Analytical investigation into magnet eddy current losses in interior permanent magnet motor using modified winding function theory accounting for pulsewidth modulation harmonics. *IEEE Trans. Magn.* **2016**, *52*, 8106805. [[CrossRef](#)]
22. Nair, S.S.; Wang, J.; Chin, R.; Chen, L.; Sun, T. Analytical prediction of 3-D magnet eddy current losses in surface mounted PM machines accounting slotting effect. *IEEE Trans. Energy Convers.* **2017**, *32*, 414–423. [[CrossRef](#)]
23. Aoyama, Y.; Miyata, K.; Ohashi, K. Simulations and experiments on eddy current in Nd-Fe-B magnet. *IEEE Trans. Magn.* **2005**, *41*, 3790–3792. [[CrossRef](#)]
24. Yamazaki, K.; Shina, M.; Miwa, M.; Hagiwara, J. Investigation of eddy current loss in divided Nd-Fe-B sintered magnets for synchronous motors due to insulation resistance and frequency. *IEEE Trans. Magn.* **2008**, *44*, 4269–4272. [[CrossRef](#)]
25. Yogal, N.; Lehrmann, C.; Henke, M. Permanent magnet eddy current loss measurement at higher frequency and temperature effects under ideal sinusoidal and non-sinusoidal external magnetic fields. In Proceedings of the IEEE Energy Conversion Congress and Exposition (ECCE), Vancouver, BC, Canada, 10–14 October 2021. [[CrossRef](#)]
26. Deak, C.; Petrovic, L.; Binder, A.; Mirzaei, M.; Irimie, D.; Funieru, B. Calculation of eddy-current losses in permanent magnets of synchronous machines. In Proceedings of the IEEE International Symposium on Power Electronics, Electrical Drives, Automation and Motion (SPEEDAM), Ischia, Italy, 11–13 June 2008. [[CrossRef](#)]
27. Plait, A.; Dubas, F. 2-D eddy-current losses model and experimental validation through thermal measurements. *IEEE Trans. Instrum. Meas.* **2022**; under review.
28. Fukuma, A.; Kanazawa, S.; Miyagi, D.; Takahashi, N. Investigation of AC loss of permanent magnet of SPM motor considering hysteresis and eddy-current losses. *IEEE Trans. Magn.* **2005**, *41*, 1964–1967. [[CrossRef](#)]
29. Kanazawa, S.; Takahashi, N.; Kubo, T. Measurement and analysis of AC loss of NdFeB sintered magnet. *Electr. Eng. Jpn.* **2006**, *154*, 869–875. [[CrossRef](#)]
30. Li, Y.; Jiang, B.; Zhang, C.; Liu, Y.; Gong, X. Eddy-current loss measurement of permanent magnetic material at different frequency. *Int. J. Appl. Electromagn. Mech.* **2019**, *61*, S13–S22. [[CrossRef](#)]
31. Fratila, R.; Benabou, A.; Tounzi, A.; Mipo, J.C. A combined experimental and finite element analysis method for the estimation of eddy-current loss in NdFeB magnets. *Sensors* **2014**, *14*, 8505–8512. [[CrossRef](#)] [[PubMed](#)]
32. Takahashi, N.; Shinagawa, H.; Miyagi, D.; Doi, Y.; Miyata, K. Analysis of eddy current losses of segmented Nd-Fe-B sintered magnets considering contact resistance. *IEEE Trans. Magn.* **2009**, *45*, 1234–1237. [[CrossRef](#)]
33. Tong, W.; Hou, M.; Sun, L.; Wu, S. Analysis and experimental verification of segmented rotor structure on rotor eddy current loss of high-speed surface-mounted permanent magnet machine. In Proceedings of the IEEE International Magnetic Conference (INTERMAG), Lyon, France, 26–30 April 2021. [[CrossRef](#)]
34. Meeker, D.C. *Finite Element Method Magnetics Ver. 4.2*. Available online: <http://www.femm.info> (accessed on 21 April 2019).
35. Asensor Technology AB, Linear High Precision Analog Hall Sensors. Available online: <https://www.asensor.eu> (accessed on 8 November 2022).
36. Plait, A.; Dubas, F. Electrical conductivity influence on eddy-current losses: Analytical study and experimental validation. In Proceedings of the IEEE International Conference on Electrical Machines and Systems (ICEMS), Gyeongju, Korea, 31 October–3 November 2021. (Best Paper Award from the IEEE ICEMS'22). [[CrossRef](#)]